Steel and Composite Structures, *Vol. 28, No. 1 (2018) 83-98*
DOI: https://doi.org/10.12989/scs.2018.28.1.083

Behavior of exterior concrete beam-column joints reinforced with Shape Memory Alloy (SMA) bars

Hossein Rezaee Azariani [a], M. Reza Esfahani [*] and Hashem Shariatmadar [b]

Department of Civil Engineering, Ferdowsi University of Mashhad, Mashhad, Iran

(*Received February 18, 2018, Revised April 20, 2018, Accepted April 24, 2018*)

Abstract. This research was conducted to study the behavior of exterior concrete beam-column joints with reinforced shape memory alloy (SMA) bars tested under cyclic loading. These bars benefit from superelastic behavior and can stand high loads without residual strains. The experimental part of the study, 8 specimens of exterior concrete beam-column joints were made and tested. Two different types of concrete with 30 and 45 MPa were used. Four specimens contained SMA bars and 4 specimens contained steel bars in beam-column joints. Furthermore, different transverse reinforcements were used in beams investigate the effects of concrete confinement. Specimens were tested under cyclic loading. Results show that SMA bars are capable of recentering to their original shape after standing large displacements. Due to the superelastic behavior of SMA bars, cracks at the joint core vanish under cyclic loading. As the cyclic loading increased, bending failure occurred in the beam outside the joint core. In the analytical parts of the study, specimens were simulated using the SeismoStruct software. Experimental and analytical results showed a satisfactory correlation. Plastic hinge length at the beam joint for specimens with SMA and steel bars was calculated by empirical equations, experimental and analytical results. It was shown that Paulay's and Priestley's equations are appropriate for concrete beam-column joints in both types of bars.

Keywords: Shape Memory Alloy (SMA); reinforced concrete; beam-column joints; superelastic effect; cyclic loading

1. Introduction

Investigation of seismic induced damage in concrete frames shows that beam-concrete joints sustain a high level of damage. Beam-column joints are among the most critical regions in reinforced concrete frames since their failure under seismic loading often leads to the partial or total collapse of the whole structure. The joints should have adequate strength and confinement to resist the cyclic loads induced by the framing members. Beam-column joint elements with steel bars in reinforced concrete structures are also highly vulnerable and considered to be a weak link in such a structural system.

Beam-column joint elements with steel bars in reinforced concrete structures are also highly vulnerable and considered to be a weak link in such a structural system. Shape memory alloy (SMA) materials have been studied for reinforcement in beam-column joints because of their ability to dissipate remarkable amounts of energy with negligible residual deformation during earthquakes. Ölander (1932) discovered superelastic behavior in Au-Cd. Chang and Read (1951) discovered reversible phase transformation in this alloy, which is the first recorded phase transformation. Using these alloys in structures has advantages and unique features such as high strength against fatigue and corrosion, recentering to the initial state and energy dissipation. Experimental studies show that these materials are unique in phase transformation as the external stress or temperature of the environment changes (Song *et al*. 2006). SAMs have two different phases acting differently including austenite and martensite. These two phases function differently at different temperatures. The austentite phase of these materials is resistant at high temperature and low stress, while martensite phase is resistant at low temperature and high stress. If the material is in the austentite phase, no residuals strain will be left after unloading, offering that this alloy is superelastic. However, when the material is in the martensite phase, there exists a residual strain that diminishes by applying temperature. In this case, SAMs show shape memory behavior. Fig. 1 shows a strain-stress behavior and phase transformations of SAMs (Seo *et al*. 2017).

Reinforced concrete frames dissipate the seismic energy by the reinforcing bars yielding. The yielding of reinforcing bars endangers the usability of these structures, because it results in residual lateral deformations. The superelastic SMAs restore the inelastic strains by stress elimination. Because SMA is a costly material, Youssef and Elfeki (2012) defined the required regions of SMA bars in a typical reinforced concrete frame to optimize its seismic performance with respect to the damage model and seismic residual deformations. They defined severities of 5 earthquakes resulting in failure to a typical reinforced concrete 6-story structure and employed them to compare 7 SMA design substitutes. Mirtaheri *et al*. (2017) studied the

*Corresponding author, Ph.D., Professor,
E-mail: esfahani@um.ac.ir
[a] Ph.D. Candidate, E-mail: rezaeeazariani@mail.um.ac.ir
[b] Associate Professor, E-mail: shariatmadar@um.ac.ir

ISSN: 1229-9367 (Print), 1598-6233 (Online)

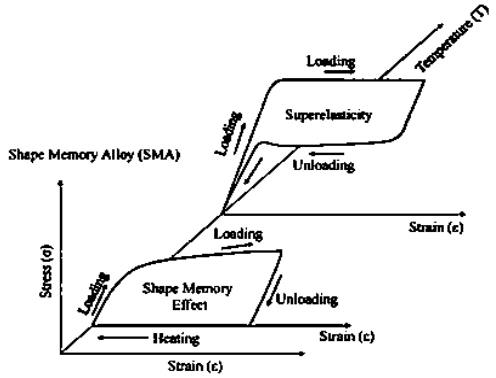

Fig. 1 Strain- stress curves for SMA (superelastic behavior and shape memory behavior)

effect of SMAs in reinforced concrete structures for buildings with different stories. Results showed that 3-story frames had almost the same spectral acceleration at failure. However, for 6 and 8-story frames, the spectral acceleration was higher for frames with steel bars. Shiravand *et al.* (2017) investigated the seismic behavior of reinforced concrete structures having SMA reinforcing bars. Various locations of SMA bars were considered in different story levels. The results showed that the structures with using SMA reinforcing bars in lower stories performed similar to those with SMA in all story levels. Elfeki and Youssef (2017) studied the use of SMA bars in reinforced concrete frames considering the horizontal seismic excitations by addressing the effect of the vertical seismic excitations. They considered a steel reinforced concrete 6-story building designed according to current seismic standards. Five different earthquake records with strong vertical components were selected for the nonlinear dynamic analysis. The results were used to evaluate the effect of the vertical excitations on the optimum positions of SMA bars. Gholampour and Ozbakkaloglu (2018) offered the results of an experimental study on the axial compressive behaviour of normal and high strength concrete (NSC and HSC) confined by SMA spirals. They applied the confining pressure to the concrete cylinders through SMA spirals that were pre-strained at 0, 5.5, and 9.5%. The test results of the SMA-confined specimens showed that the pre-strain extent of SMA spirals remarkably influenced the axial compressive behaviour of both NSC and HSC.

Alam *et al*. (2007) analyzed two concrete beam-column joints based on Canadian Standard Associations (CSA). The analysis of displacement curves of cyclic loading showed that SMA bars have better performance compared to steel bars regarding maintenance of residual strain in joints after unloading. In another study, Alam *et al*. (2008) analyzed behavior of exterior concrete beam-column joints and compared the experimental and analytical results for seismic behavior of a joint. Youssef *et al*. (2008) tested two specimens of concrete beam-column joints designed by Canadian Standards Associations. Two large-scale beam-column joints were tested under reversed cyclic loading. One specimen used only steel bars in the beam, while the other specimens used SMA bars at the plastic hinge zone in the beam and steel bars in other regions of the beam. Drifts, rotations, and energy dissipation in specimens were compared. Experimental results showed that SMA bar joints improved the deformation behavior after post-yielding deformation Alam *et al*. (2009) analyzed a seismic behavior of SMA reinforced concrete frame in two frames of 8 concrete story. One of the frames was supported only with steel bars while the other was supported by SMA bars in beam plastic hinge zone of the beam and steel bars in other regions. These two frames were located in the highly seismic region of Western Canada. The frames were analyzed by means of 10 accelerograms. Different aspects of the frame behavior were analyzed including inter-story drift, top-story drift, inter-story residual drift, and residual top-story drift. Analytical results showed that frames reinforced with SMA bars were capable of recovering most of their post-yield deformation after a strong earthquake. Alam *et al*. (2012) analyzed the behavior of 3, 6, and 8-story frames with three types of longitudinal bars in beams. The first type used steel bars in all beams, the second type used SMA bars in all plastic hinges and steel bars in other zones, and the third type used SMA bars in all beams. In all frames, steel bars were used as column reinforcement. Nonlinear dynamic time history analyses were applied using 10 earthquakes to provide the seismic requirements and capacity ratio in terms of base shear and drift for each type of frames. Analytical results showed that frames reinforced with SMA bars in low and medium rise frames have a satisfactory performance. Nehdi *et al*. (2012) tested the seismic behavior of the beam-column joints using SMA bars in the plastic-hinge zone. A reduction in residual deformation was observed in beam-column joints in the plastic-hinge zone at the end of earthquakes. Afterward, the specimen was repaired and tested in order to compare the behavior of the original and repaired joints. The two specimens demonstrated satisfactory results under reversed cyclic loading.

The present study investigates the effect of utilizing SMA bars and steel bars in exterior beam-column joints. Two types of concrete with different strengths are used in the specimens. Additionally, stirrups are applied with two different distances in order to study the effect of concrete confinement on the joint behavior. Phenomenological modeling and an analytical model proposed by Auricchio and Sacco (1997) are used for analytical modeling.

2. Test program

2.1 Specimen details

The test specimen in Fig. 2 shows an exterior beam-column joint separated from the frame structure at the points of contra-flexure. This point changes due to dynamic forces in the structures. This change does not affect joint behavior significantly due to the low displacement in the location of the beam-column the joint (Barbhuiya and Choudhury 2015). A typical 1/2 scale of exterior RC beam-column joints was designed and manufactured considering it as a 2-dimensional frame. The column pin-to-pin story height (l_c) was 360 mm, while the beam length between the loading point and the beam-joint interface was 800 mm.

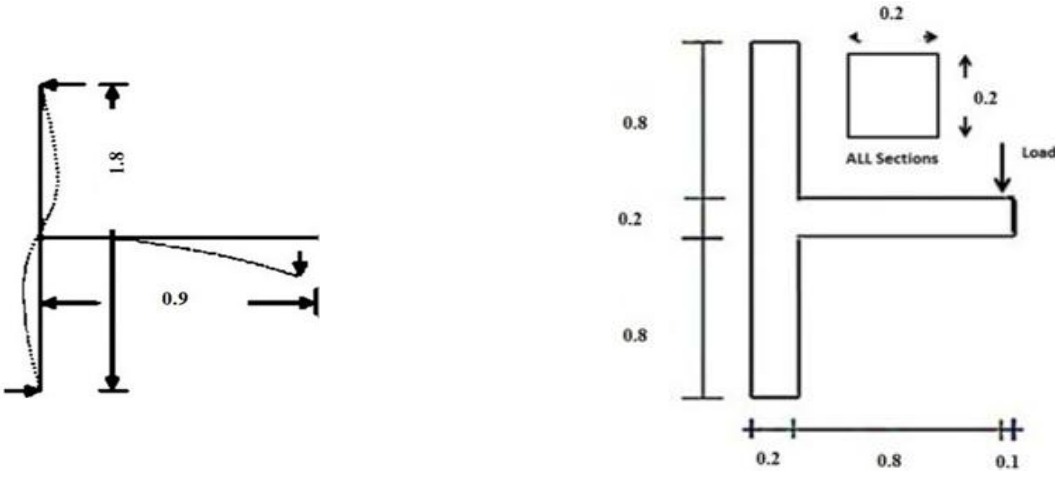

(a) Free body joint diagram (b) Geometric joint dimensions (m)

Fig. 2 RC exterior beam-column joint

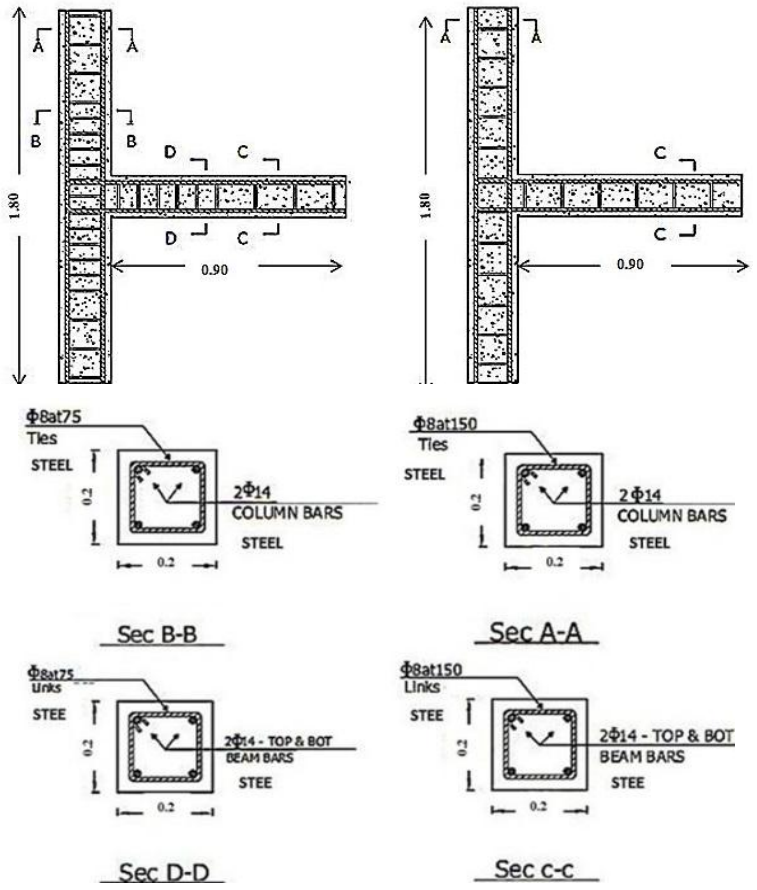

(a) For specimens 1,3 (b) For specimens 2, 4

Fig. 3 Specimens reinforced and sections with steel bars at exterior joints for specimens (m)

Eight specimens of exterior beam-column joints were manufactured and tested. Four specimens were reinforced with steel bars while four others were reinforced with SMA bars. To make specimens, two concrete types including normal concrete with design compressive strength of 30 MPa and high strength self-consolidating concrete design compressive strength of 45 MPa were used. Self-consolidating concrete was used to facilitate implementation and increase concrete strength. Table 1 provides the details and names of specimens reinforced with steel bars and SMA bars.

Fig. 3 represents specimens 1-4 with steel bars and Fig. 4 represents specimens 5-8 with SMA bars. CONF represents joint confinement and shows that stirrups

Table 1 Specimen details and symbols for normal bars and SMA bars

Specimens	Names
1	CONF_STEEL_C30
2	UNCONF_STEEL_C30
3	CONF_STEEL_C45
4	UNCONF_STEEL_C45
5	CONF_SMA_C30
6	UNCONF_SMA_C30
7	CONF_SMA_C45
8	UNCONF_SMA_C45

(transverse bars) in the beam and column are spaced 75 mm within a 2 d distance from the joint. UNCONF represents that the distance between stirrups in the beam and column is 150 mm in other regions. Steel indicates steel bars and SMA indicates SMA bars used in the beam. C30 and C45 show the concrete compressive strengths of 30 and 45 MPa, respectively. Specimen details including reinforcement arrangement bar number, and bars distance are presented in Fig. 3 for steel bar specimens and in Fig. 4 for SMA bars.

2.2 Material properties

Steel reinforcing bars with 8 mm diameter for transverse reinforcement and 14 mm for longitudinal reinforcement were used. Smooth (without ribs) SMA bars with a diameter of 14 mm were used as a longitudinal reinforcement which is Nitinol (Ni-Ti shape memory alloy). These bars were made in the austenite phase at the temperature of 10-25℃. During the experiment program, their temperature was constantly controlled by thermometers. In order to install a mechanical anchorage and apply a nut, 100 mm of SMA bars were threaded. They prevent slipping of SMA bars in the specimen. Fig. 5 shows the mechanical anchorage of SMA bars. Fig. 6 shows a stress-strain curve for steel bars and SMA bars. Table 2 presents material geometric details of specimens.

2.3 Test setup

The column of the joints was located in vertical position in the test setup. As presented in Fig. 7, a 600 kN fully hydraulic jack was used for applying cyclic loading to the end of the beam and a 200 kN load cell was used to measure the applied lateral loads to the specimens. The beam end and both ends the columns were all pin-jointed in

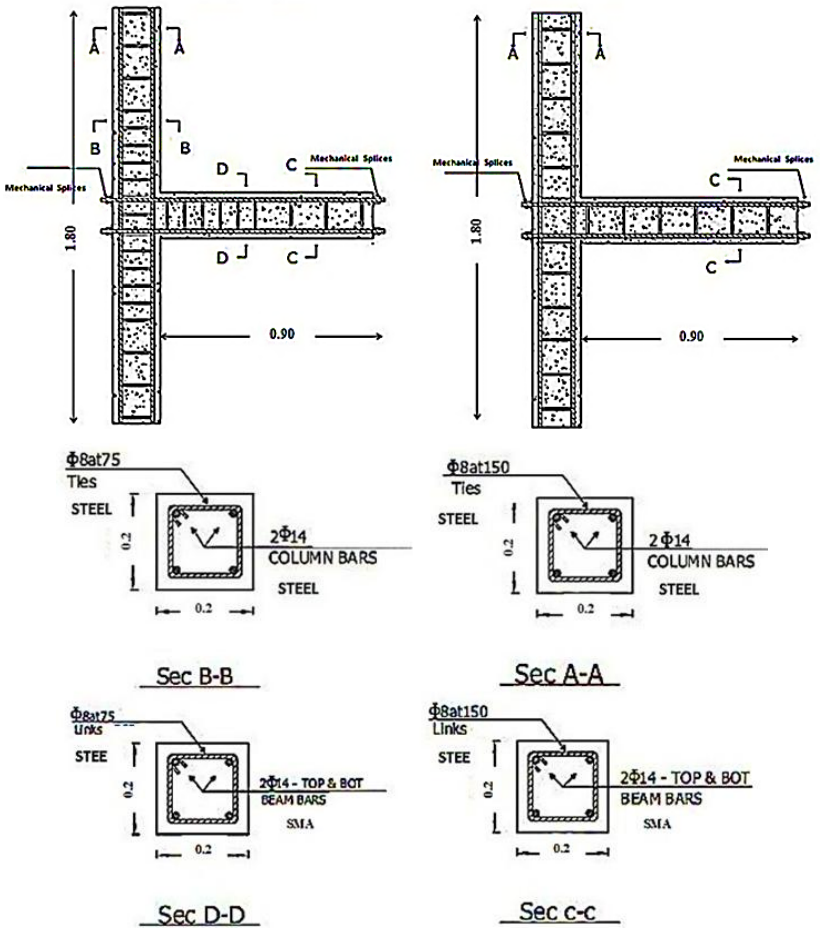

(a) For specimens 5, 7 (b) For specimens 6, 8

Fig. 4 Specimens reinforced and sections with SMA bars at the exterior joints for specimens (m)

Fig. 5 Mechanical anchorage of SMA bars

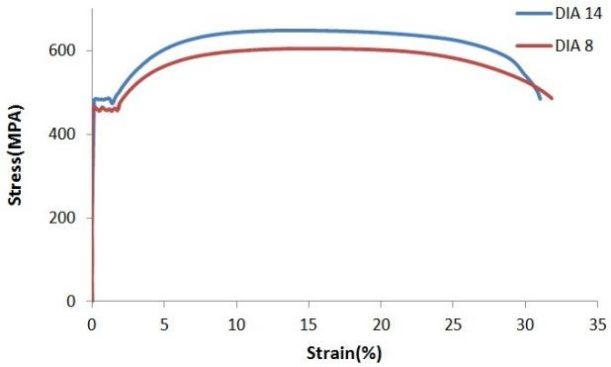

(a) Steel bars

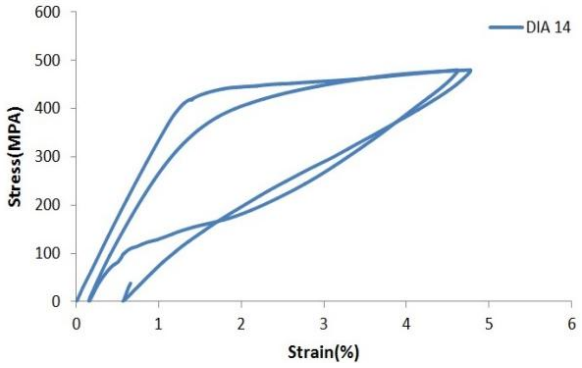

(b) SMA bars (superelastic behavior)

Fig. 6 RC exterior beam-column joint

the loading plane such that to simulate inflection points of a frame under lateral earthquake loading. Proper boundary conditions were used to simulate the actual field condition of the beam-column joint as if it was a part of the frame structure (Fig. 7). Five linear variable displacement transducers (LVDTs) were applied to measure the beam displacement at different points and calculate the curvature, accordingly. Beam tip displacement was measured by LVDT1. The beam's vertical displacement value (Δ_2) at the critical point of the beam located on 2 h distance (twice at the beam depth) from the joint core (Moehle *et al*. 2008) was measured by an LVDT2 mounted on the top of the beam. An LVDT5 mounted on beam was utilized to measure the vertical displacement of the beam close to the beam-joint interface. The LVDT3 and LVDT4 were mounted on the columns and used to calculate the rotation of the joint. Vertical displacement (Δ_5) and horizontal displacements Δ_3 and (Δ_4) were measured by LVDT5, LVDT3, and LVDT4, respectively. A data acquisition system was used to record the results during the test. Fig. 7

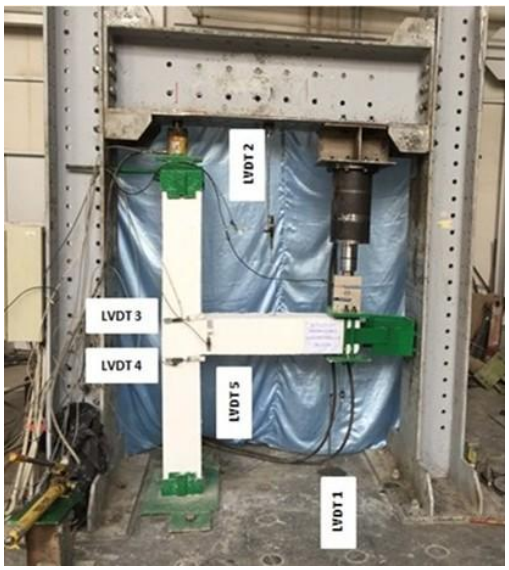

Fig. 7 Test setup together with LVDTs

Table 2 Material geometric details of specimens

	Steel		SMA	
	1,3 (CONF_*TEEL*_C30) (CONF_*STEEL*_C45)	2,4 (*UN*CONF_*STEEL*_C30) (UNCONF_*STEEL*_C45)	5,7 (CONF_*SMA*_C30) (CONF_*SMA*_C45)	6,8 (UNCONF_*SMA*_C30) (UNCONF_*SMA*_C45)
Beam				
Dimension (mm)	200 × 200	200 × 200	200 × 200	200 × 200
Longitudinal reinforcement (T&B)	4Φ14- Steel	4Φ14- Steel	4Φ14- SMA	4Φ14- SMA
Transverse reinforcement	Φ8 @75-150 (Steel)	Φ8 @150 (Steel)	Φ8 @75-150 (Steel)	Φ8 @150 (Steel)
Column				
Dimension (mm)	200 × 200	200 × 200	200 × 200	200 × 200
Longitudinal reinforcement	4Φ14-Steel	4Φ14-Steel	4Φ14-Steel	4Φ14-Steel
Transverse reinforcement	Φ8 @75-150 (Steel)	Φ8 @150 (Steel)	Φ8 @75-150 (Steel)	Φ8 @150 (Steel)

*S1: Specifications; *S2: specimens

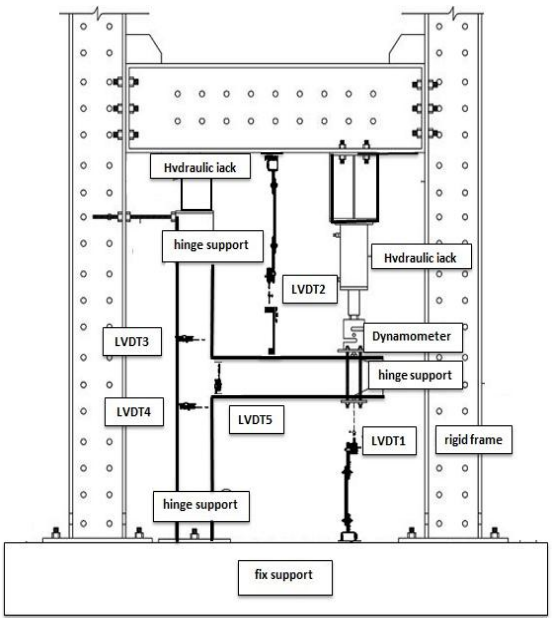

Fig. 8 Details of the test setup

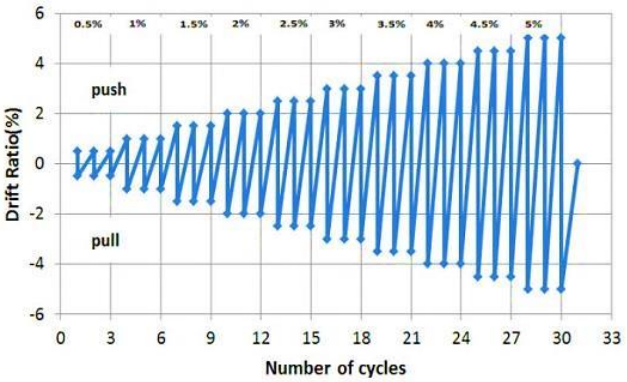

Fig. 9 Cyclic loading

shows test setup and the positioning of all the LVDTs and Fig. 8 shows details of the test setup.

Fig. 9 shows the pattern of cyclic lateral displacements caused by the hydraulic jack during each test. A total of 30 displacement cycles were statically applied up to a 5% drift. Similar to much previous research (Hakuto *et al*. 2000, Ghobarah and El-Amoury 2005), the loading was applied on a load control method followed by a displacement control method. A hydraulic jack was used to apply a constant axial compression force to the columns during testing. The force was about 10% of the column maximum strength (120 kN) and was kept constant during the test.

3. Experimental study

3.1 Load-story drift

The relations between the story drift and beam tip load are shown in Figs. 10 and 11 for steel and SMA bar specimens, respectively. Figures are plotted up to the point that the story drift reaches 4%. As shown in specimens 1-4, stiffness and strength of the beam-Column Joint have changed in each cycle of loading. In a specific drift, the load of the beam tip maximized in the specimens and then decreased in the next circles. Comparison of the hysteresis

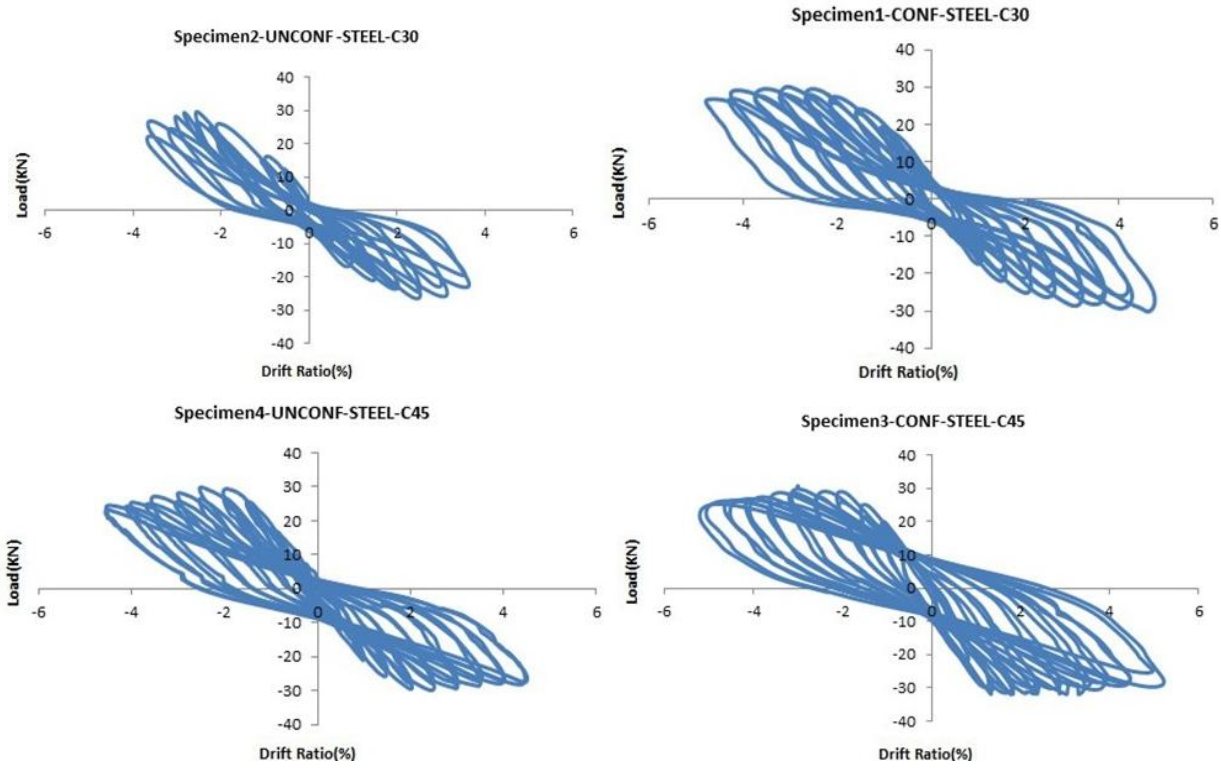

Fig. 10 Load-drift curve of the beam tip in steel bar specimens

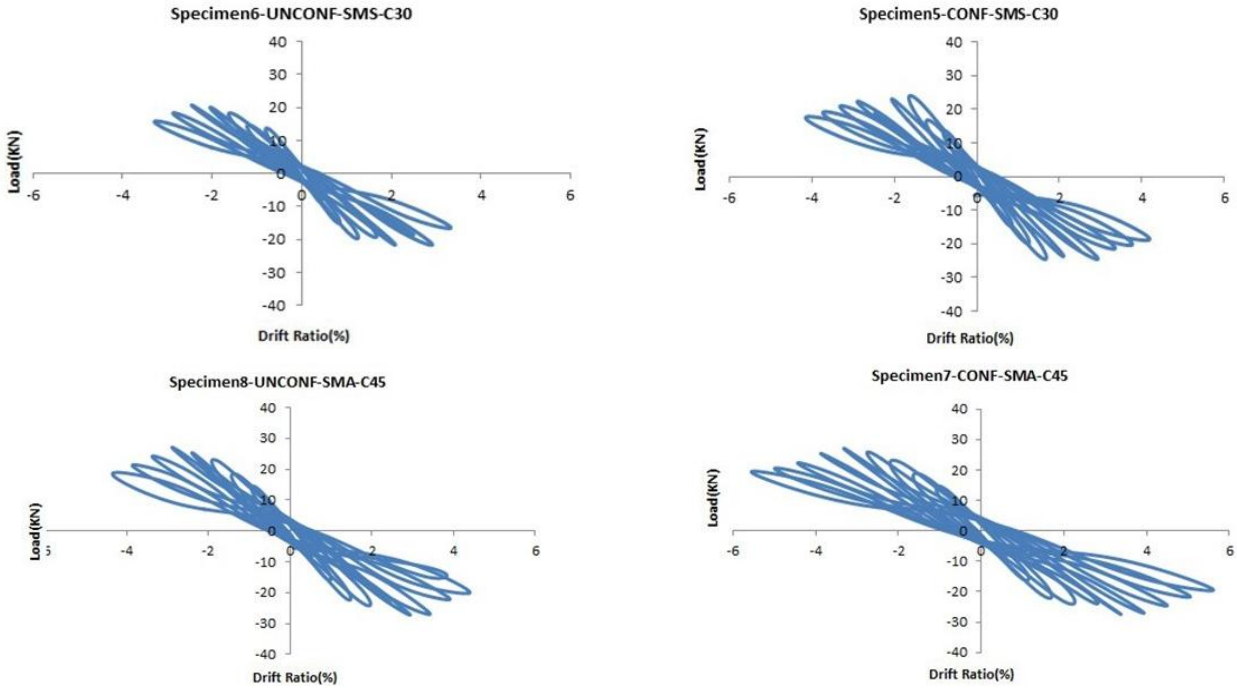

Fig. 11 Load-drift curve of the beam tip in SMA bar specimens

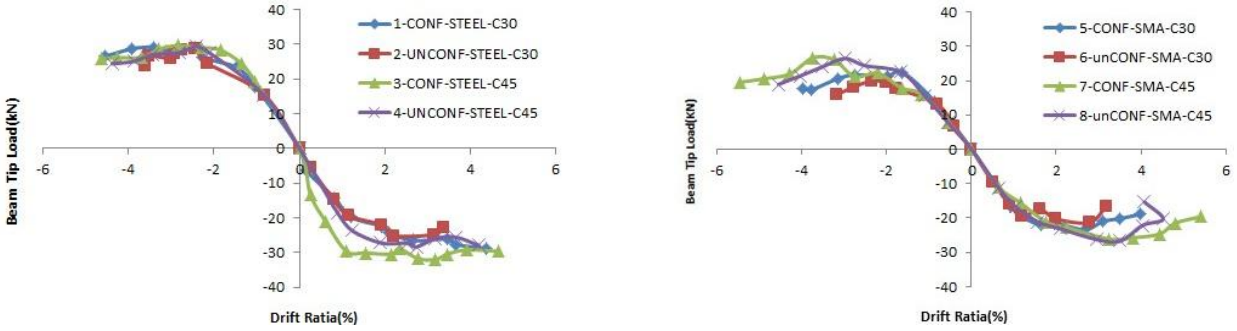

(a) Steel (b) SMA

Fig. 12 Load-story drift envelopes of specimens

loops shows that pinching effect in the confined specimen with high strength concrete (Specimen 3). Pinching effect has the highest value in the unconfined specimen with normal concrete (Specimen 2), whereas in specimens with SMA bar these changes are not significant. The maximum load used to the beam tip load for specimens with steel bar was approximately 30 kN at a drift of 2-3%, whereas specimens with SMA bar could stand 24-28 kN of beam tip load at the same drift as specimens with a steel bar. As presented in Fig. 11, in specimens 5-8, the residual displacement left in the beam is much less than that of specimens with steel bars (specimens 1-4) due to the superelastic behavior of SMAs, which allows these materials to sustain large deformation even after unloading. Considerable permanent deformation was created in the reinforcement of beam tip in specimens 1-4.

3.2 Load-story drift envelopes

Fig. 12 shows the beam-tip load versus story drift envelope of all the specimens. The seismic performance of beam-column joints was evaluated in accordance with ACI Committee (2005). Accordingly, in order to attain desired performance in a moment frame, the joint should meet three criteria. Firstly, to secure the failure criteria in the third cycle with the drift of 3.5%, the maximum load should not be less than 75% of the lateral strength in the same side as the load is being applied. Secondly, the relative energy dissipation ratio should not be less than 0.125. Thirdly, the secant stiffness about zero drift, which is calculated as the secant stiffness from a drift of 0.35% to a drift of 0.35%, should not be less than 0.05 times as the primary stiffness recorded during the first cycle. According to Fig. 12, by fulfilling all acceptation criteria, the performance of the specimens was deemed satisfactory.

3.3 Cracking patterns

Figs. 13 and 14 show cracking patterns at 5% drift for a specimen with steel and SMA bars, respectively. As Fig. 14

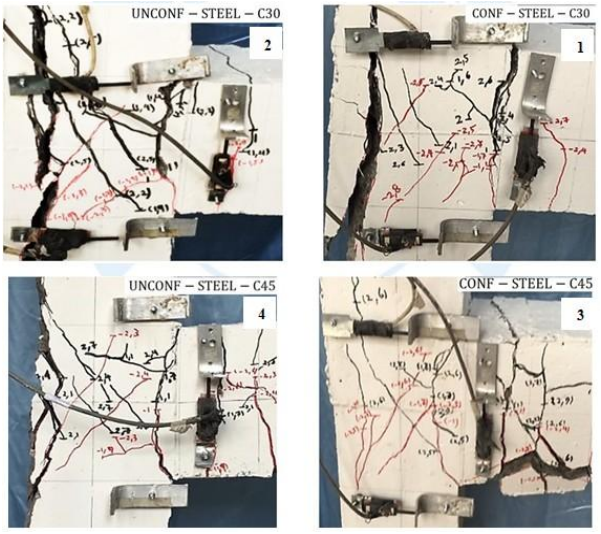

Fig. 13 cracking patterns in steel bar specimens

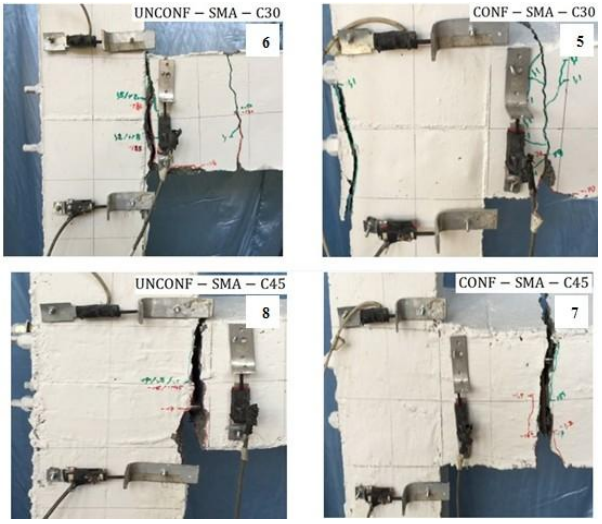

Fig. 14 cracking patterns in SMA bars specimens

shows, in beam-column joints with steel bars and low strength concrete, in confined and unconfined specimens (specimens 1 and 2, respectively), shear failure occurred in the joint core. By increasing concrete strength in confined and unconfined specimens (specimen 3 and 4, respectively) bending failure occurred in the beam outside of the joint core. Cracks width in confined specimens with low and high strength concrete (specimens 1 and 3) is smaller than that of unconfined specimens (specimens 2 and 4).

As can be seen from Fig. 14, in specimens 6 and 8 reinforced with SMA bars, cracking was not significant at the joint core, and bending failure occurred in the beam. Furthermore, in specimens 5 and 7, the beam confinement results in increasing the distance between the joint core and the point that failure occurs.

3.4 Energy dissipation

Energy dissipation is the most important factors in the seismic design of structures. The advantage of any detailing design is in the energy level dissipated by the structural component provided with such a detailing design (Murty *et al*. 2003). The energy dissipation during a specific loading cycle is determined as the area enclosed within the load versus displacement curve, starting and ending with a zero displacement (Alameddine and Ehsani 1991). The capacity of a structure to stabilize an earthquake depends on its ability to dissipate the energy input. Although it is difficult to evaluate such an energy input during an earthquake, a satisfactory design should guarantee a larger energy dissipation capability of the structure compared to the demand. The cumulative energy dissipated by the beam-column joint specimens with steel and SMA bars, during the reversed cyclic load tests, was determined by summing the energy dissipated in load-displacement loops through the test. Steel specimens had the higher energy dissipation capacity. Figs. 15(a) and (b) show cumulative dissipation energy versus drift in specimens with steel and SMA bars. It can be observed from the energy dissipation plots (Fig. 15(a)) that the specimens with steel bars had about twice higher cumulative energy dissipation capacity than that of the specimen with SMA bars. This difference is because of the large hysteretic loop of steel compared to that of the superelastic effect SMA material. The least energy dissipation occurred in specimen 2 with steel bars, though the highest pinching effect in cycles is the highest. Increasing concrete strength recovers the hysteresis loops, leading to the highest energy dissipation in specimen 3. In specimen 7 with SMA bars, up to a 2% drift, energy

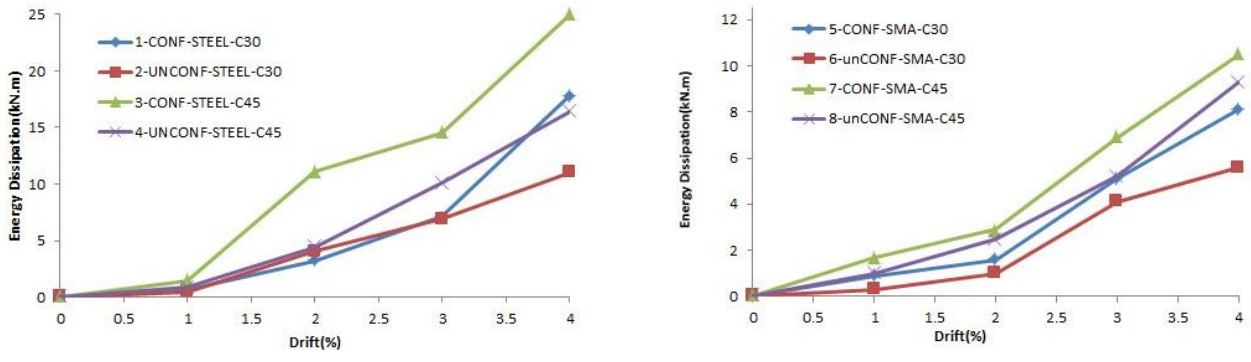

(a) Steel (b) SMA

Fig. 15 Cumulative dissipated energy-drift curve in specimens

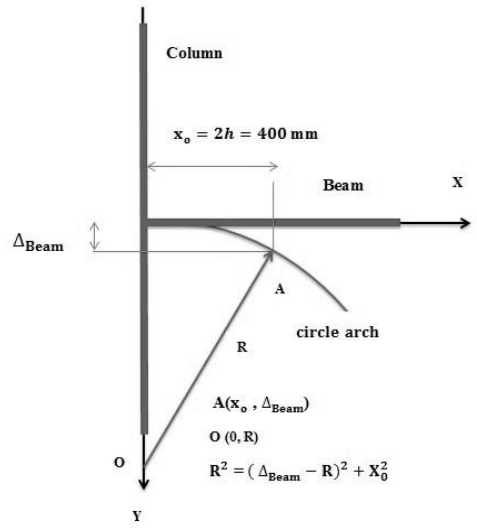

Fig. 16 Circular deformation of beam-column joint

dissipation is similar to that of other specimens (specimens 5, 6, and 8), but in the drifts from 2 to 3% energy dissipation decreased in these specimens probably due to the slip of bars in concrete. In specimens reinforced with SMA bars, as shown in Fig. 16 (section 3.1), the residual displacement after unloading is much less than that of the specimens with steel bars and SMAs have the ability to regain their initial form after withstanding plastic deformation.

3.5 Moment-curvature relationships

Curvature (1/R) can be calculated by assuming beam deformation in the critical point as a circle arch. The circle radius (R) and curvature (1/R) in the critical section of the beam can be calculated by Eqs. (1)-(3). Fig. 16 shows circular deformation and details of beam-column joint for calculation Δ_{Beam} (mm).

$$(\Delta_{Beam} - R)^2 + X_0^2 = R^2 \quad (1)$$

$$R = \frac{\Delta_{Beam}^2 + X_0^2}{2\Delta_{Beam}} \quad (2)$$

$$\phi = \frac{1}{R} \quad (3)$$

$$\theta_c = \frac{\Delta 4 - \Delta 3}{L} \quad (4)$$

$$\Delta 0 = \Delta 2 - \Delta 5 \quad (5)$$

$$\Delta_{Beam} = \Delta 0 - \theta_c \times 2h \quad (6)$$

In the specimens, x_o = 400 mm is the critical length of the beam between the place of LVDT2 and the face of the column and ∅ is the curvature of the beam's section. As described in Section 2.3 and presented Figs. 7 and 8, the vertical displacement of the beam joint (Δ_2) is measured by LVDT2 in the critical region of the beam, while vertical displacement (Δ_5) is measured by LVDT5. Moreover, Δ_3 and (Δ_4) horizontal displacements are measured by LVDT3 and LVDT4, respectively. θ_c is the rotation of the joint node measured by LVDT2 and LVDT5 and Δ_0 is displacement measured by LVDT2 and LVDT5 using Eq. (4) and Eq. (5). L is the distance between two horizontal LVDTs (3 and 4) installed on the column that is 300 mm for all specimens. Displacement of all beams was approximately 2 h from the joint core, which is shown by Δ_{Beam} and can be calculated by Eq. (6). In this equation, h (beam height) is 200 mm.

Based on Eqs. (1)-(6), the moment-curvature relationships of specimens with steel bars and SMA bars are shown in Fig. 17. Fig. 17(a) shows that the moment-curvature relationship continues linearly until it reaches the steel yield point in the steel bars of specimens 1 to 4. When the steel bars yield, the curvatures increase but the moments do not change, significantly. In these specimens, all curves show similar behavior for the moment of 14 kNm.

Additionally, increasing strength and confinement in specimen 3 increases the curvature than other specimens. Fig. 17(b) shows that in specimens 5-8 with SMA bars, the moment-curvature relationship continues linearly until reaching the SMA yield point. When SMA yields, the curvature increases. It is of note that the moment value in these specimens is less than that of specimens with steel bars. All curves behave similarly up to a moment of 10 kN/m. Confinement in specimen 5 increases curvature

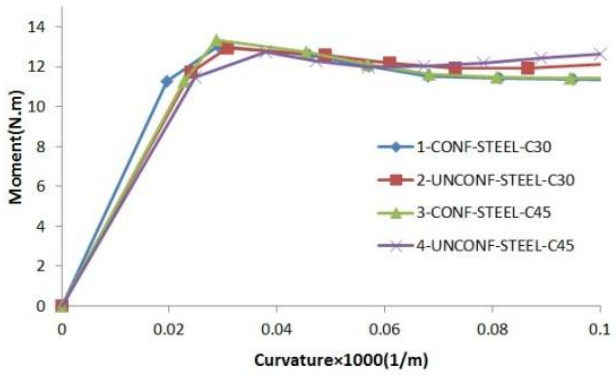

(a) Steel

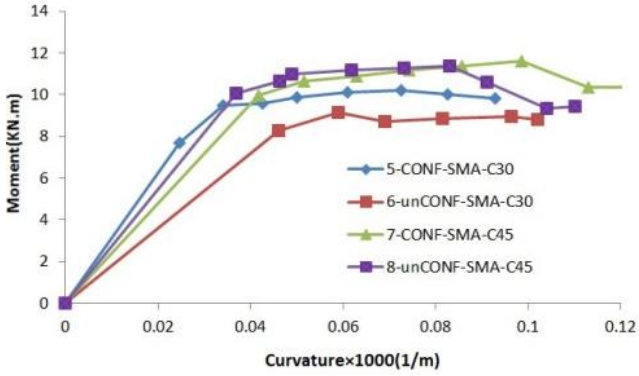

(b) SMA

Fig. 17 Moment-curvature relationships of specimens

compared to specimen 6. Moreover, increasing the strength and confinement of concrete in specimen 7 leads to an increase in curvature more than that of other specimens.

4. Analytical study

In the analytical part of this study, SeismoStruct software was used to analyze concrete joints based on cyclic loading. This software is capable of considering nonlinear geometric behavior and nonlinear behavior of materials and can predict frame behavior under static and dynamic loading in large displacements. This software is appropriate to model different materials such as concrete, steel, FRP, and SMA due to its efficiency and precision (SeismoStruct Help File 2016).

4.1 Modeling concrete materials

The most efficient model for concrete stress-strain based on SeismoStruct software under cyclic loading is the model proposed by Mander *et al*. (1988). Fig. 18 shows the stress-strain diagram of confined and unconfined concrete under cyclic loading. In this model, compressive stress of concrete f'_c is defined by Eq. (7) that includes the branches of the stress-strain curve. The parameters in the equation are derived from Eqs. (8) and (13) (SeismoStruct Help File 2016).

In Eqs. (7)-(13), f'_{co} is the strength of unconfined concrete, f'_{cc} is the strength of confined concrete, k is the ratio of the strength of confined concrete to unconfined one, and *k* for the reinforced concrete members is 1-2. In SeismoStruct software, ε_{cc} is the compressive strain along specimen length in the confined concrete,ε_{co} is the strain corresponding to the strength of unconfined concrete, E_c is the concrete modulus of elasticity, E_{sec} is the secant modulus of the concrete, and r is the modulus of elasticity ratio. In this software, concrete tensile strength (f_t) is calculated by $f_t = K_t \times \sqrt{f'_c}$, where K_t ranges from 0.5 for direct tensile stress to 0.75 concrete under bending (Mander *et al*. 1988). Concrete specific weight is 24 kN/m^3.

$$f'_c = \frac{f'_{cc}\, xr}{r - 1 + x^r} \tag{7}$$

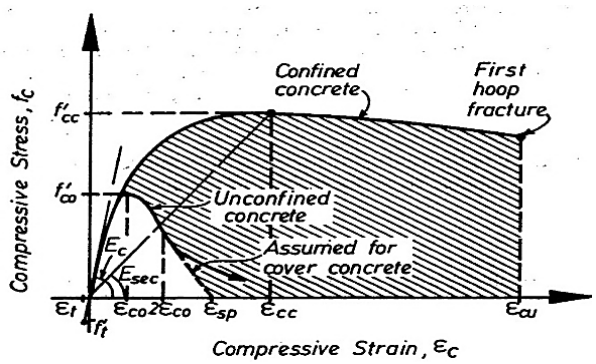

Fig. 18 Stress-strain curve of confined and unconfined concretes under cyclic loading

$$x = \frac{\varepsilon_{co}}{\varepsilon_{cc}} \tag{8}$$

$$f'_{cc} = k f'_{co} \tag{9}$$

$$\varepsilon_{cc} = \varepsilon_{co}\left[1 + 5\left(\frac{f'_{cc}}{f'_{co}} - 1\right)\right] \tag{10}$$

$$E_c = 5000\sqrt{f'_{co}} \tag{11}$$

$$E_{\text{sec}} = \frac{f'_{co}}{\varepsilon_{cc}} \tag{12}$$

$$r = \frac{E_c}{E_c - E_{\text{sec}}} \tag{13}$$

4.2 Modeling reinforcing bars

The axial behavior models proposed by Auricchio and Sacco (1997), Menegotto and Pinto (1973) were used for beams and columns for specimens with SMA and steel bars, respectively. Auricchio and Sacco model was the super-elastic model used in the FE program where SMA was subjected to reverse cyclic loadings under stress-induced transformation. Menegotto and Pinto (1973) model was used for beams and columns for specimens with steel bars. Modulus of elasticity of specimens with steel and SMA bars were considered to be 200,000 and 83,000 MPa, respectively.

4.3 Geometric modeling and structural analysis

In this study, beams are divided into 2 elements, and columns are divided into 4 elements. The method used for joint analysis was static-time history analysis. Properties of elements in SeismoStruct were defined in element classes module. The reason of using different elements was to define the properties of the similar element or different sections and materials. To select frame element, inelastic force-based plastic hinge frame element type was used. After defining element properties for making and joining elements in modeling, Element Connectivity module was used. Structure geometry in SeismoStruct was defined in a three-step process. First, all structural and non-structural nodes were defined. Then, the method for joining elements was defined and element connectivity could be determined. Finally, restraints modules were determined by the boundary elements conditions (SeismoStruct Help File 2016). Finite elements model of the specimens is shown in Fig. 19. In this regard, Figs. 19(a), (b), and (c) illustrate the specifications of nodes, members, and joint modeling, respectively.

4.4 Results of analysis

The model presented by Auricchio and Sacco (1997) is used to examine the behavior of specimens with SMA bars. The analysis model is shown in Fig. 20(b). In Fig. 20(a), the

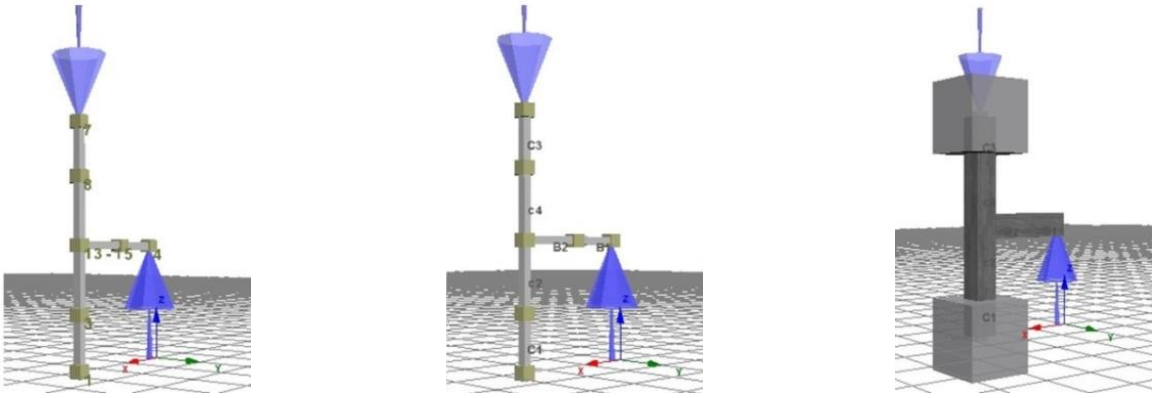

(a) Specifications of nodes (b) Specifications of members (c) Joint modeling

Fig. 19 Finite elements model of specimens

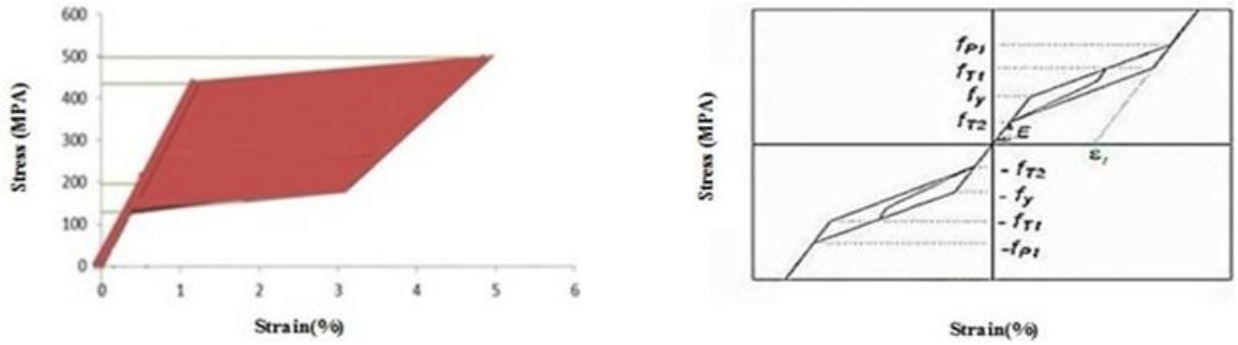

(a) Based on experimental results (b) Model based on Auricchio and Sacco (1997)

Fig. 20 Superelastic behavior of SMA bars

Table 2 Material geometric details of specimens

	Steel		SMA	
	1,2 (CONF_*STEEL*_C30) (UNCONF_*STEEL*_C30)	3,4 (CONF_*STEEL*_C45) (UNCONF_*STEEL*_C45)	5,6 (CONF_*SMA*_C30) (UNCONF_*SMA*_C30)	7,8 (CONF_*SMA*_C45) UNCONF_*SMA*_C45)
Concrete	NC	SCC	NC	SCC
Compressive strength (MPa)	30.1	45.4	30.1	45.4
Steel (longitudinal)				
Yield strength (MPa)	484	484	550	550
Ultimate strength (MPa)	649	649	1100	1100
Young's modulus (GPa)	202.4	202.4	83	83
Stirrups (transverse)				
Yield strength (MPa)	463	463	463	463
Ultimate strength (MPa)	605	605	605	605
Young's modulus (GPa)	202.4	202.4	202.4	202.4
SMA				
f_y (σ_{Ms}) (MPa)	-	-	430	430
f_{P1} (σ_{Mf}) (MPa)	-	-	500	500
f_{T1} (σ_{As}) (MPa)	-	-	200	200
f_{T2} (σ_{Af}) (MPa)	-	-	120	120
SE plateau strain (ε_l) (%)	-	-	4	4

*S1: Specifications; *S2: specimens

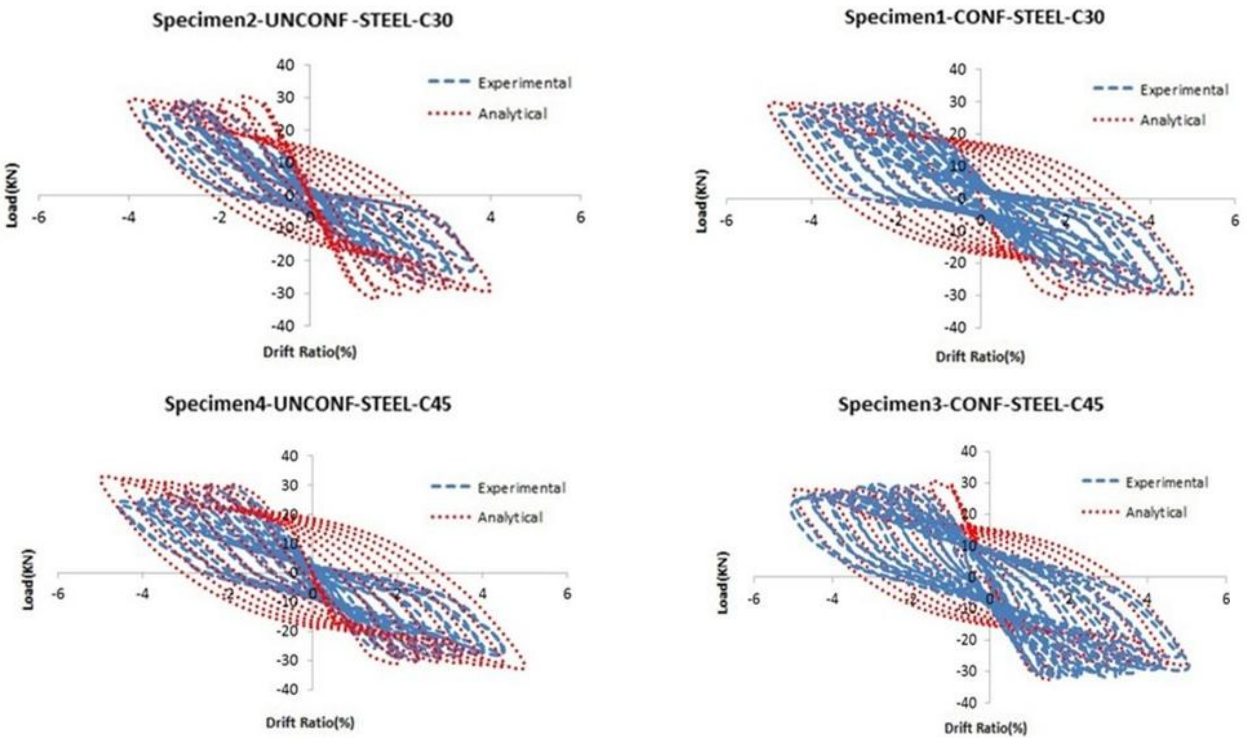

Fig. 21 Comparison of analytical and experimental results of the beam tip drift-load curve in steel bar specimens

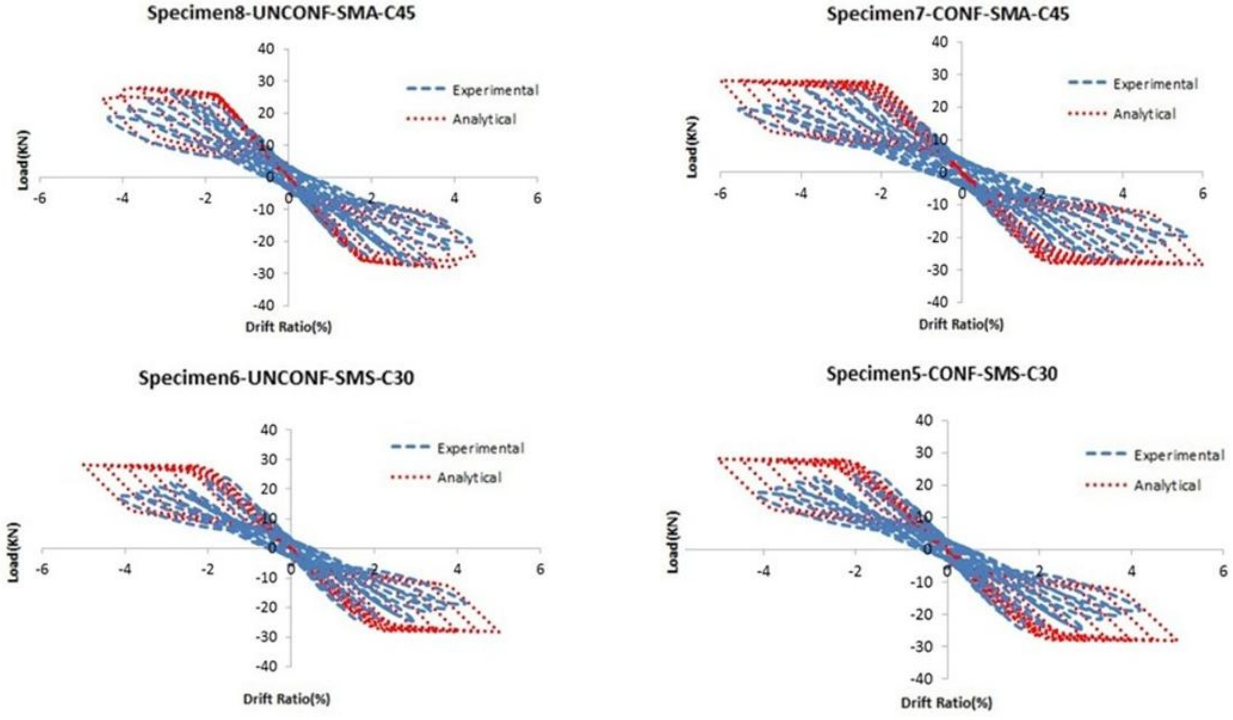

Fig. 22 Comparison of analytical and experimental results of the beam tip drift-load curve in SMA bar specimens

model is presented based on experimental results. The hysteretic stress-strain curve of superelastic behavior for specimens with SMA bars showed a flag-shaped displacement hysteretic shape. In the analysis model, f_y (σ_{Ms}) is austenite to martensite starting stress behavior, f_{P1} (σ_{Mf}) is austenite to martensite finishing stress behavior, f_{T1} (σ_{As}) is martensite to austenite starting stress behavior, f_{T2} (σ_{Af}) is martensite to austenite finishing stress behavior, and ε_l is superelastic plateau strain length or maximum residual strain. Table 3 shows detailed material properties of specimens.

Figs. 21 and 22 compare the analytical and experimental

results of the beam tip drift-load curve with steel and SMA bar specimens. The analytical and experimental results of the specimens show a good correlation. As presented in Fig. 21, the pinching effect has a considerable impact on specimens with steel bars and low strength concrete. The best correlation between analytical and experimental results can be seen in specimen 3. Considering the decrease in stiffness and strength as well as slipping of the longitudinal bars in the specimens, the pinching effect cannot be avoided. The greatest pinching effect occurs in the specimen 2, and specimen 3 is the one with the lowest pinching effect. In the numerical models of the hysteresis loops related to beam-column joints, reduction of stiffness and strength as well as the pinching effect are calculated with errors. Therefore, some discrepancies can be observed between experimental and analytical results. Similar observation has been reported by previous researchers (Yu 2006). As shown in Fig. 22 and based on both experimental and analytical results, it can be stated that the specimens with SMA bars have the ability to regain their initial form even after sustaining plastic deformation.

In Table 4, a summary of the experimental and analytical results is presented for all specimens. In this table, $f_c^{'}$ is the concrete strength, P_u is ultimate load, P_y is the load corresponding to yielding of the beam longitudinal bars, δ_u and δ_y are the beam tip drift. In the experimental part, cyclic loading was applied to the beam tip of all specimens to determine ultimate loads, yield loads, and their drifts. The analytical values are presented in Table 4 based on SeismoStruct software. Comparison of the experimental results in Table 4 shows that in specimens with steel and SMA bars yielding of longitudinal bars (specimens 3 and 7) occurred at 19.62 and 13.65 kN with drifts of 1.04% and 1.52%, respectively. The ultimate load carting capacity was recorded at 30.73 and 27.45 kN with a drift of 3.01% and 3.05 for specimens with steel and SMA bars, respectively. Furthermore, reviewing the analytical results in Table 4 shows that the values recorded as P_y for specimens with steel and SMA bars (specimens 3 and 7) were 30.01 and 19.3 kN at drifts of 1% and 1.24%, respectively. The ultimate load carrying capacity was 32.14 and 28.10 kN for specimens with steel and SMA bars at drifts of 3% and 3.9%, respectively. Comparison of the results acquired based on analytical and experimental studies shows a reasonable correlation between them.

Table 5 presents a comparison between experimental and numerical results for specimens with steel and SMA bars. For all the experimental specimens, the average value

Table 4 Experimental and analytical results of specimens (steel and SMA bars)

Specimens	$f_c^{'}$ (MPa)	Experimental				Analytical			
		P_y (kN)	δ_y (%)	P_u (kN)	δ_u (%)	P_y (kN)	δ_y (%)	P_u (kN)	δ_u (%)
1	30	18.51	0.88	29.74	2.99	18.74	1.20	31.38	3.00
2	30	16.50	0.83	26.52	2.46	18.13	1.00	31.21	2.50
3	45	19.62	1.04	30.73	3.01	30.01	1.00	32.14	3.00
4	45	19.22	0.90	29.88	2.50	20.11	0.90	30.08	2.80
5	30	13.23	1.47	24.59	2.73	18.20	1.16	28.02	2.86
6	30	12.43	1.38	20.72	2.30	15.92	1.02	27.82	0.39
7	45	13.65	1.52	27.45	3.05	19.3	1.24	28.10	3.90
8	45	13.57	1.51	27.26	3.03	19.23	1.16	27.90	3.41

Table 5 Comparison between experimental and analytical results

Specimens	$f_c^{'}$ (MPa)	Experimental / Analytical			
		P_{y-Exp}/P_{y-Ana}	$\delta_{y-Exp}/\delta_{y-Ana}$	P_{u-Exp}/P_{u-Ana}	$\delta_{u-Exp}/\delta_{u-Ana}$
1	30	0.99	0.73	0.95	1.00
2	30	0.91	0.83	0.85	0.98
3	45	0.65	1.04	0.96	1.00
4	45	0.96	1.00	0.99	0.89
Average	-	0.88	0.90	0.94	0.97
Standard deviation	-	0.16	0.15	0.06	0.05
5	30	0.73	1.27	0.88	0.95
6	30	0.78	1.35	0.74	0.96
7	45	0.71	1.23	0.98	0.78
8	45	0.71	1.30	0.98	0.89
Average	-	0.73	1.29	0.90	0.90
Standard deviation	-	0.03	0.05	0.11	0.08

Table 6 Calculation of plastic hinge length in the beam based on empirical equations

Specimens	d_b	d	L	f_y	Empirical			
					L_p(Eq. (14))	L_p(Eq. (15))	L_p(Eq. (16))	L_p(Eq. (17))
	mm	mm	mm	MPa	mm	mm	mm	mm
1- 4 (steel bars)	13.90	200	900	484	118	164	52	220
5- 8 (SMA bars)	14.05	200	900	550	118	164	52	242

length in mm, d_b is the diameter of longitudinal bars in mm,

Table 7 Calculation of plastic hinge length in the beam based on experimental and analytical

S*	Experimental					Analytical				
	Δ_y	Δ_u	$\emptyset_y$	$\emptyset_u$	L_p(Eq. 19)	Δ_y	Δ_u	$\emptyset_y$	$\emptyset_u$	L_p(Eq. 19)
	mm	mm	Rad/km	Rad/km	mm	mm	mm	Rad/km	Rad/km	mm
1	7.9	26.9	19.6	123.0	235	10.80	27.00	22	142	165
2	7.5	22.1	24.0	100.8	244	9.00	22.50	27	116	188
3	9.4	27.1	22.8	121.6	227	9.00	27.00	25	141	193
4	8.1	22.5	24.7	100.0	246	8.10	25.20	28	115	254
5	7.3	26.3	24.6	95.0	380	10.44	25.74	27	109	239
6	8.2	22.1	46.0	102.0	340	9.18	21.51	53	115	257
7	9.7	30.4	42.0	129.0	322	11.16	35.01	48	148	323
8	8.5	26.4	37.0	110.0	335	10.44	30.69	42	127	322

*S: specimens

and standard deviation for the ratio of experimental to analytical results for load and deflection are presented in columns 3 to 6. It can be seen that the analytical results are in good correlation with experimental results.

5. Calculation of plastic hinge length

Plastic hinge length of a structural member is a basic parameter to evaluate structural response and the damage caused by seismic loads. Various empirical equations have been presented to calculate the plastic hinge length of reinforced concrete members. In many equations, plastic hinge length is proportionate to the effective depth of the member section, member length, diameter, and yield stress of the bars (Abdel-Fattah and Wight 1987). Some empirical equations proposed by Sawyer (1964), Corley (1966), Mattock (1967), Paulay and Priestley (1992) are presented in Eqs. (14)-(17), respectively.

$$L_p = 0.075L + 0.25d \tag{14}$$

$$L_p = 0.5d + \frac{L}{\sqrt{d}} \tag{15}$$

$$L_p = 0.05L + 0.5d_b \tag{16}$$

$$L_p = 0.08L + 0.022d_b f_y \tag{17}$$

Where d and L are effective beam depth and beam and f_y is the yield stress of longitudinal bars in MPa. Table 6 presents the calculation of plastic hinge length based on empirical Eqs. (14)-(17). Empirical Eqs. (16) and (17) estimate the least and the most values for plastic hinge length, respectively.

In the experimental and analytical results, plastic hinge length can be calculated by Eqs. (18) and (19) (Alam *et al*. 2008). In these equations, Δ_u and Δ_y are the ultimate displacements and yield displacements of the beam, and $\emptyset_u$ and $\emptyset_y$ are the ultimate curvatures and yield curvatures of the beam, respectively. Table 7 presents calculations of plastic hinge length based on Eqs. (18) and (19) and experimental and analytical results.

$$\Delta p = \Delta u - \Delta y \tag{18}$$

$$\Delta p = (\varphi_u - \varphi_y) L p \left(L - \frac{L p}{2} \right) \tag{19}$$

Comparison of the experimental results based on Table 7 reveals that the values of $\emptyset_y$ for specimens with steel and SMA bars (specimens 3 and 7) are 22.8 and 42 Rad/km and the values for $\emptyset_u$ are 121.6 and 129 Rad/km, respectively. Moreover, reviewing the analytical results in Table 7 shows that the values of $\emptyset_y$ for specimens with steel and SMA bars (specimens 3 and 7) are 25 and 48 Rad/km and the values for $\emptyset_u$ are 141 and 148 Rad/km, respectively. Comparison of the analytical and experimental results of the

curvature calculated at a distance of 2h from the joint core shows an acceptable correlation between these results.

Comparing Paulay and Priestley empirical Eq. (17) with the experimental and analytical results in Tables 5 and 6 shows that the empirical equation Eq. (17) is appropriate for a plastic hinge length prediction bars in concrete joints.

6. Conclusions

In this study, SMA bars were studied as reinforcing bars with unique optimal behavior for controlling beam-column joints under cyclic loadings. In the experimental part of the study, 8 specimens of concrete beam-column joints with SMA and steel bars were tested. The behavior of the specimens was also analyzed by SeismoStruct software. Based on the results of the study, the following conclusions are drawn:

- Experimental results showed that the specimens with SMA bars had appropriate energy dissipation. However, the dissipation of energy of these specimens was 50% less than of the specimen with steel bars. Although energy dissipation of specimens with SMA bars is less than that of steel bars, their superelastic behavior can stand high load without remaining residuals strains.
- Beam tip drift-load curves of all SMA bar specimens show the high ability of the materials to recentering to their initial shape after tolerating large displace-ents. The residual displacement of specimens with SMA bars is much less than that of steel bars and specimens returned to their initial shape after standing significant plastic deformations.
- In specimens with SMA bars, in both cases of normal and high-strength concretes, cracks were not significant at the joint core and cyclic loading removed the cracks at the joint core. As the cyclic load increased, bending failure occurred outside the joint core along the beam length. The increase in the confinement of the beam moved the failure point far from the joint core. In beam-column joints with steel bars, shear failure occurred in the beam-column joint core. However, as the concrete strength and confinement increased, bending failure occurred in beam outside the joint core.
- In specimens with SMA bars, in both cases of normal and high-strength concretes, cracks were not significant at the joint core and cyclic loading removed the cracks at the joint core. As the cyclic load increased, bending failure occurred outside the joint core along the beam length. The increase in the confinement of the beam moved the failure point far from the joint core. In beam-column joints with steel bars, shear failure occurred in the beam-column joint core. However, as the concrete strength and confinement increased, bending failure occurred in beam outside the joint core.
- Plastic hinge length at the beam in beam-column joints for SMA bars and steel bars was calculated empirical equations, experimental and analytical results. It was shown that Paulay's and Priestley's equations effectively predict the plastic hinge length in concrete beam-column joints.
- Specimens were analyzed by SeismoStruct finite element software. Comparison between analytical and experimental results of the beam tip drift-load curve showed a good correlation in all specimens.

References

Abdel-Fattah, B. and Wight, J.K. (1987), "Study of moving beam plastic hinging zones for earthquake-resistant design of RC buildings", *Struct. J.*, **84**(1), 31-39.

ACI Committee (2005), Acceptance criteria for moment frames based on structural testing and commentary (ACI 374.1-05); American Concrete Institute, Farmington Hills, MI, USA.

Alam, M.S., Nehdi, M. and Youssef, M.A. (2007), "Applications of shape memory alloys in earthquake engineering", *Proceedings of the 9th Canadian Conference on Earthquake Engineering*, Ontario, Canada, June.

Alam, M.S., Youssef, M.A. and Nehdi, M. (2008), "Analytical prediction of the seismic behavior of superelastic shape memory alloy reinforced concrete elements", *Eng. Struct.*, **30**(12), 3399-3411.

Alam, M.S., Youssef, M.A. and Nehdi, M.A. (2009), "Seismic performance of concrete frame structures reinforced with superelastic shape memory alloys", *Smart Struct Syst., Int. J.*, **5**(5), 565-585.

Alam, M.S., Moni, M. and Tesfamariam, S. (2012), "Seismic overstrength and ductility of concrete buildings reinforced with superelastic shape memory alloy rebar", *Eng. Struct.*, **34**, 8-20.

Alameddine, F. and Ehsani, M.R. (1991), "High-Strength RC connections subjected to inelastic cyclic loading", *J. Struct. Eng.*, **117**(3), 829-850.

Auricchio, F. and Sacco, E. (1997), "A superelastic shape-memory-alloy beam model", *J. Intel. Mater. Syst. Struct.*, **8**(6), 489-501.

Barbhuiya, S. and Choudhury, A.M. (2015), "A study on the size effect of RC beam-column connections under cyclic loading", *Eng. Struct.*, **95**, 1-7.

Chang, L.C. and Read, T.A. (1951), "Plastic deformation and diffusionless phase changes in metals-the gold-cadmium beta phase", *JOM*, **3**(1), 47-52.

Corley, W. (1966), "Rotational capacity of reinforced concrete beams", *J. Struct. Div.*, **92**(5), 121-126.

Elfeki, M.A. and Youssef, M.A. (2017), "Shape memory alloy reinforced concrete frames vulnerable to strong vertical excitations", *J. Build. Eng.*, **13**, 272-290.

Ghobarah, A. and El-Amoury, T. (2005), "Seismic rehabilitation of deficient exterior concrete frame joints", *J. Compos. Constr.*, **9**(5), 408-416.

Gholampour, A. and Ozbakkaloglu, T. (2018), "Confinement of normal-and high-strength concrete by Shape Memory Alloy (SMA) Spirals", *IOP Conference Series*: *Materials Science and Engineering*, **301**(1), 012056.

Hakuto, S., Park, R. and Tanaka, H. (2000), "Seismic load tests on interior and exterior beam-column join with substandard reinforcing details", *Struct. J.*, **97**(1), 11-25.

Mander, J.B., Priestley, M.J.N. and Park, R. (1988), "Observed the stress-strain behavior of confined concrete", *J. Struct. Eng.*, **114**(8), 1827-1849.

Mattock, A.H. (1967), "Discussion of rotational capacity of reinforced concrete beams by W. Gene Corley", *J. Struct. Div.*, **93**(2), 519-522.

Menegotto, M. and Pinto, P.E. (1973), "Method of analysis for

cyclically loaded RC plane frames including changes in geometry and non-elastic behavior of elements under combined normal force and bending", Preliminary Report; IABSE, Zurich, Switzerland.
Mirtaheri, M., Amini, M. and Khorshidi, H. (2017), "Incremental dynamic analyses of concrete buildings reinforced with shape memory alloy", *Steel Compos. Struct., Int. J.*, **23**(1), 95-105.
Moehle, J., Hooper, J. and Lubke, C. (2008), "NEHRP Seismic Design Technical Brief No. 1-Seismic Design of Reinforced Concrete Special Moment Frames: A Guide for Practicing Engineers", No. Grant/Contract Reports (NISTGCR)-08-917-1; U.S. Department of Commerce.
Murty, C.V.R., Rai, D.C., Bajpai, K.K. and Jain, S.K. (2003), "Effectiveness of reinforcement details in exterior reinforced concrete beam-column joints for earthquake resistance", *ACI Struct. J.*, **100**(2), 149-156.
Nehdi, M., Alam, M.S. and Youssef, M.A. (2012), "Seismic behavior of repaired superelastic shape memory alloy reinforced concrete beam-column joint", *Smart Struct. Syst., Int. J.*, **7**(5), 329-348.
Ölander, A. (1932), "The crystal structure of AuCd", *Zeitschrift für Kristallographie-Crystalline Materials*, **83**(1-6), 145-148.
Paulay, T. and Priestley, M.N. (1992), *Seismic Design of Reinforced Concrete and Masonry Buildings*, John Wiley & Sons, Inc., New York, NY, USA.
Sawyer, H.A. (1964), "Design of concrete frames for two failure stages", *Special Publication*, **12**, 405-431.
SeismoStruct Help File (2016), Version 7.0.4., Piazza Castello, Italy. URL: http://www.seismosoft.com
Seo, J., Hu, J.W. and Kim, K.H. (2017), "Analytical investigation of the cyclic behavior of smart recentering t-stub components with superelastic SMA bolts", *Metals*, **7**(10), 386.
Shiravand, M.R., Nashtaee, M.A. and Veismoradi, S. (2017), "Seismic assessment of concrete buildings reinforced with shape memory alloy materials in different stories", *Struct. Des. Tall Special Build.*, **26**(15).
Song, G., Ma, N. and Li, H.N. (2006), "Applications of shape memory alloys in civil structures", *Eng. Struct.*, **28**(9), 1266-1274.
Youssef, M.A. and Elfeki, M.A. (2012), "Seismic performance of concrete frames reinforced with superelastic shape memory alloys", *Smart Struct. Syst., Int. J.*, **9**(4), 313-333.
Youssef, M.A., Alam, M.S. and Nehdi, M. (2008), "Experimental investigation on the seismic behavior of beam-column joints reinforced with superelastic shape memory alloys", *J. Earthq. Eng.*, **12**(7), 1205-1222.
Yu, W. (2006), "Inelastic modeling of reinforcing bars and blind analysis of the benchmark tests on beam column joints under cyclic loading", Ph.D. Dissertation; Rose School–European School for Advanced Studies in Reduction of Seismic Risk, University of Pavia, Italy.

BU